https://doi.org/10.5194/egusphere-2025-5852
Preprint. Discussion started: 11 December 2025

# The Spatial and Temporal Distribution Patterns of $XCH_4$ in Iran: New Insights from TROPOMI Observations

Ali Rahimi[1], Manuchehr Farajzadeh[1], Yousef Ghavidel[1], and Christoffer Karoff[2]

[1] Department of Physical Geography, Tarbiat Modares University, Tehran, 14155-4838, Iran
[2] Department of Geoscience, Aarhus University, Aarhus, 8000 Aarhus C, Denmark

*Correspondence to:* Christoffer Karoff (email: karoff@geo.au.dk), Manuchehr Farajzadeh (email: farajzam@modares.ac.ir)

**Abstract.** The unprecedented increase in methane concentration, as the second most important greenhouse gas after carbon dioxide, poses a serious challenge to climate change mitigation policies, while accurate and comprehensive monitoring remains insufficient in many countries, including Iran. This study investigates the spatial and temporal patterns of column-averaged methane in Iran using satellite-based observations from Tropospheric Monitoring Instrument on the Sentinel-5P satellite during 2019–2024 and compares them with data from the Emissions Database for Global Atmospheric Research database. On average, $XCH_4$ concentrations across Iran increased from 1872.6 ± 11.9 ppb in 2019 to 1918.6 ± 11.2 ppb in 2024, representing a +46.1 ± 16.4 ppb rise over six years. All uncertainty estimates represent standard deviations, with a mean value of 12.3 ppb. Statistical and spatial analyses, including Global Moran's I (0.914–0.982, $p < 0.01$), Local Moran's I, and the Getis-Ord Gi* hotspot analysis, confirmed that methane concentrations in Iran exhibit a significant clustering pattern. Hotspots were mainly observed in Class 1: Northern Agro-Hotspots (Gilan, Mazandaran, and Golestan), Class 2: Central Urban-Dense Hotspots, and Class 3: Southern Industrial-Fossil Hotspots, whereas Class 4: Low-Emission Provinces and Class 5: Very-Low-Emission Provinces exhibited lower concentrations with sparse hotspots, located mostly in western and eastern Iran. The highest seasonal averages were recorded in summer (1914.3 ± 13.1 ppb) and autumn (1910.5 ± 13.5 ppb). Comparison with EDGAR data indicates that several major emission sources are underestimated, and spatial overlaps with the observed hotspots did not exceed 5% in any month. Satellite observations reveal discrepancies in hotspot locations and emission magnitudes, emphasizing that relying solely on modeled inventories may misrepresent methane emissions.

## 1 Introduction

Climate change has emerged as one of the most critical and complex global challenges of the 21st century, primarily driven by the unprecedented rise in atmospheric concentrations of greenhouse gases as a result of anthropogenic activities ( Saleem et al., 2025). Scientific assessments and international reports, particularly from the Intergovernmental Panel on Climate Change (IPCC), have confirmed that major greenhouse gases, namely carbon dioxide, methane and nitrous oxide, are significantly intensifying the greenhouse effect, global warming, and destabilization of climatic systems (Qin et al., 2025; Xing et al., 2024).

Among these gases, methane ($CH_4$) ranks as the second most influential anthropogenic greenhouse gas after $CO_2$. Despite its lower atmospheric concentration, $CH_4$ exhibits a significantly higher global warming potential (GWP). Over a 20-year period, methane is estimated to be more than 80 times more potent than carbon dioxide in trapping heat (Zhang et al., 2022; Jackson et al., 2024; South et al., 2024; Subraveti and Anantharaman, 2025; Lerner., 2025). Given its high GWP and relatively short atmospheric lifetime of 9 ± 1.9 years (Prather et al., 2012), methane has become a critical target for near-term climate mitigation strategies (Saunois et al., 2019).

Methane emissions originate from both natural and anthropogenic sources. Natural emissions account for approximately 38% globally, including wetlands, organic-rich soils, and geological seepage (Kirschke et al., 2013). Anthropogenic activities, such as fossil fuel extraction (~35% of global $CH_4$ emissions), agriculture (~20%), and waste management (~7–8%), are responsible for over 60% of global $CH_4$ emissions and dominate the remainder (Saunois et al., 2019; Lorente et al., 2021; Hernández et al., 2025). This dominance of anthropogenic sources has made methane a central focus of climate policy and scientific research.

The concentration of atmospheric methane has increased substantially since the industrial revolution, rising from ~720 ppb in 1750 to 1896 ppb in 2021, corresponding to an average annual increase of ~5 ppb globally (Meyer et al., 2022; NOAA, 2025). This upward trend has persisted in recent years, with methane levels exceeding 1927 ppb in April 2025 (NOAA, 2025).

Regional methane concentrations in the Middle East are slightly elevated compared to the global mean, ranging between 1895 and 1915 ppb, primarily due to the region's extensive oil and natural gas reserves (Alcibahy et al., 2025). Given the accelerating rise of GHGs in the atmosphere and their undeniable role in climate change, there is an urgent need for more accurate and comprehensive monitoring of methane emissions across temporal and spatial scales (Zhang et al., 2016; Liu et al., 2020; Johnson et al., 2021). Two main approaches are used to monitor methane: top-down and bottom-up. The top-down approach generally involves remote sensing technologies, including satellite-based observations, while the bottom-up approach relies on ground-based measurements, emission inventories, and statistical data (Du et al., 2024). Each approach offers unique advantages and limitations, but integrated methodologies can provide a more robust understanding of methane emission dynamics.

Accurate identification of emission sources and their spatial-temporal patterns is essential for improving climate models and developing targeted mitigation policies (Güğül et al., 2023). Moreover, enhancing methane monitoring at national and sub-national levels will enable better risk assessments, more effective emission reduction strategies, and stronger contributions to global climate commitments.

Scattered studies have investigated methane and other GHG emissions in Iran, often focusing on specific sources or sectors. Localized studies measured emissions from particular infrastructures or cities. For instance, Afshoun et al. (2022) quantified fugitive $CH_4$ emissions from the natural gas distribution network in Mashhad, identifying end-user systems as the dominant contributors. Industrial wastewater in Iran has been identified as an important local source of greenhouse gas emissions. Nayeb et al. (2020) highlighted that the industrial wastewater sector contributes significantly to methane and carbon dioxide emissions, with treatment plants in industrial parks and the food processing and paper industries being major contributors. Municipal landfills were also highlighted as significant local methane sources. Talaiekhozani and Nasiri (2016) emphasized their role as important contributors to regional greenhouse gas emissions. At the national scale, Mahdavian et al. (2025) analyzed the relationship between $CH_4$ emissions, climate, and livestock production, highlighting the impacts of rising temperatures and land use on food security. Maazallahi et al. (2025) detected 110 emission sources from oil, gas, and waste infrastructures using satellite observations, estimating over 6 million metric tons of $CH_4$ emissions from Oil and Gas and about 3.8 million metric tons from waste annually. Mousavi et al. (2020) examined spatiotemporal $CH_4$ distributions across Iran in 2013 using GOSAT satellite data and ordinary kriging, showing higher concentrations in southern and eastern regions influenced by flaring sites, temperature, land surface characteristics, and atmospheric transport. Correlations with environmental variables indicated that $CH_4$ concentrations increased with higher land surface and air temperature and decreased with higher vegetation cover (NDVI) and humidity, showing clear seasonal and regional patterns. While insightful, these efforts remain fragmented and sector-specific, highlighting the need for integrated, nationwide assessments of methane emissions.

https://doi.org/10.5194/egusphere-2025-5852
Preprint. Discussion started: 11 December 2025

In this study, satellite-based remote sensing using the TROPOspheric Monitoring Instrument (TROPOMI) sensor aboard the Sentinel-5P satellite was employed to address the absence of a comprehensive ground-based monitoring infrastructure in Iran. The analysis focused on determining the spatial and temporal distribution of methane across the country, with the aim of identifying emission hotspots and major source regions. In parallel, monthly sector-specific grid maps from the Emissions Database for Global Atmospheric Research (EDGAR) v8.1 database were examined to provide a bottom-up perspective on methane emissions. To achieve this, statistical and geospatial analyses were applied to detect patterns and trends in methane concentrations.

## 2 Materials and Methods

### 2.1 Study Area

The study area of this research is the Islamic Republic of Iran, located in Southwest Asia between 24° and 40° North latitude and 44° and 64° East longitude. Iran encompasses a total area of approximately 1,645,195 square kilometers, making it the second-largest country in the Middle East, divided administratively into 31 provinces and more than 1,200 counties. It ranks as the 18th most populous nation globally, with a population of nearly 80 million in 2016, with ~23% residing in urban centers and ~77% in rural areas. The country exhibits highly diverse physiographic features, including prominent mountain ranges such as the Alborz (~20,000 km²) and Zagros (~400,000 km²), extensive central deserts (e.g., Dasht-e Kavir 77,600 km² and Dasht-e Lut 51,800 km²), fertile plains, and coastal zones along the Caspian Sea (~20,000 km²), Persian Gulf (~8,000 km²), and Gulf of Oman (~3,500 km²). The mean elevation across the country is about 1,200 meters above sea level (Figure S1).

Iran is predominantly dry, with over 82% of its land classified as arid or semi-arid (Atlantic Council, 2025). More comprehensive climate classification studies, using Köppen-Geiger, Feddema, and UNEP schemes, indicate that over 98% of the country undergoes climates ranging from arid to sub-humid (Raziei, 2022). UNEP's breakdown reveals that approximately 52.9% of Iran is arid, 34.3% semi-arid, and 6.9% dry, cumulatively covering around 94%, while humid and sub-humid zones occupy the remaining ~6% (UNEP, 2022). Annual precipitation varies from <60 mm in hyper-arid central zones (~25% of the land) to >1,500 mm in the humid southwestern Caspian coastal region (~1% of the land) (Darand, 2025). Mean annual temperatures range between 13.2°C in the northwestern highlands and 25.4°C in the southwestern lowlands, with seasonal extremes of −15°C in winter to >45°C in summer, influenced by elevation and regional atmospheric patterns (Najafi et al., 2023). These climatic variables are critical determinants of vegetation dynamics, evapotranspiration, and soil moisture, which in turn affect the transport, dispersion, and atmospheric lifetime of trace gases such as methane.

Land use and land cover (LULC) in Iran is markedly diverse, encompassing approximately 20.9 ± 2.1 million hectares of agricultural land, nearly 13% of the national territory. Of this, irrigated lands (including orchards) account for about 10.2 ± 1.08 million hectares, while rainfed agriculture comprises 10.7 ± 1.02 million hectares. Agricultural zones are predominantly concentrated in basins with moderate to humid climatic conditions (Karimi et al., 2025).

Iran is a major emitter of atmospheric methane in the region, mainly because of its extensive fossil fuel extraction industry, intensive agricultural activities, and expanding anthropogenic sources such as waste and transportation.

According to EDGAR data, Iran's $CO_2$ and total greenhouse gas emissions have increased steadily over the past three decades. Total $CO_2$ emissions rose from roughly 205 million tons in 1990 to 690 million tons in 2020, while per-capita $CO_2$ emissions increased from 3.6 t/person to 8.3 t/person. Total GHG emissions followed a similar upward trend, reaching over 900 million tons $CO_2$-equivalent by 2018. The $CO_2$ intensity relative to GDP also increased from 0.42 t $CO_2$/kUSD in 1990 to 0.66 t $CO_2$/kUSD in

https://doi.org/10.5194/egusphere-2025-5852
Preprint. Discussion started: 11 December 2025

2020, indicating that economic growth has remained closely linked to carbon emissions. These trends underscore the dominant role of the energy and industrial sectors in shaping Iran's greenhouse gas profile. Integrating emission inventories with sectoral and satellite-based data can provide a more accurate understanding of spatiotemporal emission patterns and support low-carbon development planning (Table S1) (Crippa et al., 2023).

This complex interaction between physiographic variability, climate conditions, and methane-intensive human activities makes Iran a strategically important region for investigating the spatiotemporal distribution of column-averaged methane concentrations ($XCH_4$).

## 2.2 Data Source

### 2.2.1 TROPOMI Observations

The primary dataset in this study is the atmospheric methane product from TROPOMI, a high-resolution imaging spectrometer onboard the Sentinel-5P satellite, launched by the European Space Agency (ESA) in October 2017 (Ghosh and Manna, 2025). TROPOMI measures multiple spectral bands: ultraviolet (UV) and visible (VIS, 270–500 nm), near-infrared (NIR, 675–775 nm), and shortwave infrared (SWIR, 2305–2385 nm), optimized for detecting $XCH_4$ and other trace gases (Tu et al., 2025). Its native spatial resolution was 7 × 7 km² at the beginning of the mission and was improved to 7 × 5.5 km² from August 6, 2019, to enhance detection capabilities (Karoff et al., 2023).

The satellite follows a sun-synchronous orbit with a local overpass time around 13:30 LT. This configuration minimizes diurnal variation in measurements (Van Geffen et al., 2022). We used the Level 3 gridded and bias-corrected $XCH_4$ product via Google Earth Engine (GEE), covering 2019–2024 (6 years) across Iran.

To study seasonal patterns, data were grouped by climatological seasons Winter (DJF, ~90 days), Spring (MAM, ~92 days), Summer (JJA, ~92 days), and Autumn (SON, ~91 days). This method, widely used in climate sciences by organizations like IPCC, NOAA, and ECMWF, allows meaningful temporal comparisons (IPCC, 2013; NOAA, n.d.; ECMWF, n.d.). Seasonal composites represent mean $XCH_4$ concentrations across valid pixels in each grid cell (covering ~95% of valid pixels per grid cell). This ensures spatial comparability and temporal consistency, crucial for identifying trends and emission hotspots.

### 2.2.2 EDGAR v8.1 Modeled Emissions

EDGAR is one of the most comprehensive and widely used global inventories of anthropogenic greenhouse gas emissions. Its latest release, EDGAR version 8.1 (v8.1, 2022), provides high-resolution gridded data at a spatial resolution of 0.1° × 0.1° (~10 km) with monthly temporal coverage, covering major anthropogenic sources including fossil fuel exploitation, agriculture (such as enteric fermentation and rice cultivation), waste management, industrial combustion, transportation, power generation, and residential buildings.

In Iran, total methane ($CH_4$) emissions increased steadily from roughly 125 million t in 2019 to 158 million t in 2023, corresponding to a growth of ~26% over five years. Per-capita emissions also rose from about 1.6 t $CH_4$/person in 2019 to 2.0 t $CH_4$/person in 2023. Sectoral analysis shows that fossil fuel exploitation is the dominant source, increasing from around 101 million t in 2019 to 128 million t in 2023, accounting for ~80% of total $CH_4$ in 2019 and ~81% in 2023. Agriculture contributed approximately 17% in 2019 and ~15% in 2023, while transport accounted for ~2%, and buildings, industrial combustion, power industry, and processes combined made up the remaining ~1–2% (Table S2) (Crippa et al., 2023).

https://doi.org/10.5194/egusphere-2025-5852
Preprint. Discussion started: 11 December 2025

The steady increase in emissions, particularly from fossil fuel exploitation, underscores the critical role of the energy sector in Iran's methane budget. Comparison of EDGAR modeled data with TROPOMI satellite observations enables the evaluation of spatial emission patterns, identification of hotspot discrepancies, and assessment of the strengths and limitations of modeled inventories for regional monitoring. Integrating bottom-up inventories with satellite-based measurements provides a complementary framework for understanding the spatiotemporal dynamics of methane emissions at national and sub-national scales.

### 2.3 Data Processing Method

### 2.3.1 Global Spatial Autocorrelation Analysis (Global Moran's I)

To quantify the overall spatial structure of $CH_4$ concentrations across the study area, Global Moran's I was calculated for each year and for the entire study period. This index measures spatial autocorrelation by assessing both the attribute similarity ($CH_4$ concentration values) and spatial proximity of features. The formula for Global Moran's I is (1):

$$I = \frac{n}{W}\frac{\sum_{i=1}^{n}\sum_{j=1}^{n} w_{ij}(x_i-\bar{x})(x_j-\bar{x})}{\sum_{i=1}^{n}(x_i-\bar{x})^2} \tag{1}$$

In this equation, n is the total number of spatial units (e.g., grid cells), $x_i$ and $x_j$ are the $CH_4$ concentrations at locations i and j, and x̄ is the mean $CH_4$ concentration across all locations. The term $w_{ij}$ represents the spatial weight between units i and j, defined based on an 8-nearest neighbor queen contiguity approach with row-standardization such that $\sum_j w_{ij}$=1. W is the sum of all spatial weights.

The value of Moran's I ranges from −1 to +1. A value greater than zero indicates positive spatial autocorrelation, meaning similar $CH_4$ values are clustered together geographically. A value less than zero suggests negative spatial autocorrelation, where dissimilar values are more likely to be adjacent. Values close to zero imply spatial randomness with no meaningful spatial dependency. To test the statistical significance of the observed Moran's I, 999 random permutations were performed, and Z-scores and pseudo p-values were computed to assess whether the observed spatial patterns significantly deviate from randomness.

### 2.3.2 Local Spatial Autocorrelation Analysis (Local Moran's I)

To identify localized spatial clusters and outliers of $CH_4$ concentrations within the study area, Anselin's Local Moran's I statistic was applied. This local indicator of spatial association (LISA) evaluates the extent to which individual observations are similar or dissimilar to their spatial neighbors, thereby enabling the detection of statistically significant hot and cold spots, as well as spatial outliers.

The local statistic is calculated as (2):

$$I_i = \frac{(x_i-\bar{x})}{m^2}\sum_{j=1}^{n} w_{ij}\left(x_j - \bar{x}\right) \tag{2}$$

Where Ii is the Local Moran's I value for location i; xi and xj represent the $CH_4$ concentrations at spatial locations i and j, respectively; x̄ denotes the global mean $CH_4$ concentration; and wij is the spatial weight between locations i and j. The term $m^2$ refers to the mean of the squared deviations from the global mean, serving as a normalization factor.

Based on the calculated Local Moran's I values and their statistical significance, each spatial unit can be classified into distinct cluster types that reveal the local spatial structure of $CH_4$ concentrations. A High–High (HH) cluster indicates a location with high $CH_4$ values surrounded by similarly high values, representing a hotspot. Conversely, a Low–Low (LL) cluster reflects a coldspot, where low values are adjacent to other low values. High–Low (HL) and Low–High (LH) categories identify spatial outliers, where a high value is surrounded by low values or vice versa. These classifications provide valuable insights into local spatial dynamics and assist in pinpointing regions with elevated emissions or anomalous patterns that may warrant further investigation.

#### 2.3.3 Hotspot Analysis (Getis-Ord Gi*)

To further quantify spatial clusters of high or low $CH_4$ concentrations, the Getis-Ord Gi* statistic was used (3):

$$G_i^* = \frac{\sum_{j=1}^{n} w_{ij}\,(x_j - \bar{X})}{S\sqrt{\frac{n\sum_{j=1}^{n} w_{ij}^2 - (\sum_{j=1}^{n} w_{ij})^2}{n-1}}} \tag{3}$$

In this formula, xj is the $CH_4$ value at location j, and X̄ represents the mean $CH_4$ value across all spatial units (not the standard deviation). The term S refers to the mean standard deviation of all $CH_4$ values, while wij indicates the spatial weight between locations i and j. The variable n is the total number of spatial units. A high positive Z-score (Z(Gi)*) with a low p-value indicates a statistically significant hotspot, whereas a low negative Z-score suggests a coldspot. In this study, spatial clusters with $|Z| > 1.96$ and $p < 0.05$ were considered statistically significant at the 95% confidence level.

## 3 Results

### 3.1 Spatial Distribution of XCH4 in Iran

#### 3.1.1 Spatial Statistical Characterization

The preliminary analysis of satellite-derived methane data across Iran revealed consistently high emission levels. Annual mean $XCH_4$ concentrations, derived from TROPOMI observations, increased from 1873 ppb in 2019 to 1919 ppb in 2024, with minimum values ranging from 1741 ppb in 2019 to 1779 ppb in 2024, and maximum values spanning 1975–2051 ppb. The observed standard deviations varied between 10.98 ppb in 2022 and 14.03 ppb in 2021, with a mean standard deviation of 12.3 ppb, reflecting moderate spatial variability across the country. Figure 1 illustrates the annual variations of column-averaged methane over Iran during the period 2019–2024. Panel (a) shows the spatial distribution of $XCH_4$ derived from TROPOMI, clearly identifying regions with elevated methane concentrations. Panel (b) presents the statistical distribution of the data as histograms, highlighting the changes in annual mean, median, and variability.

https://doi.org/10.5194/egusphere-2025-5852
Preprint. Discussion started: 11 December 2025

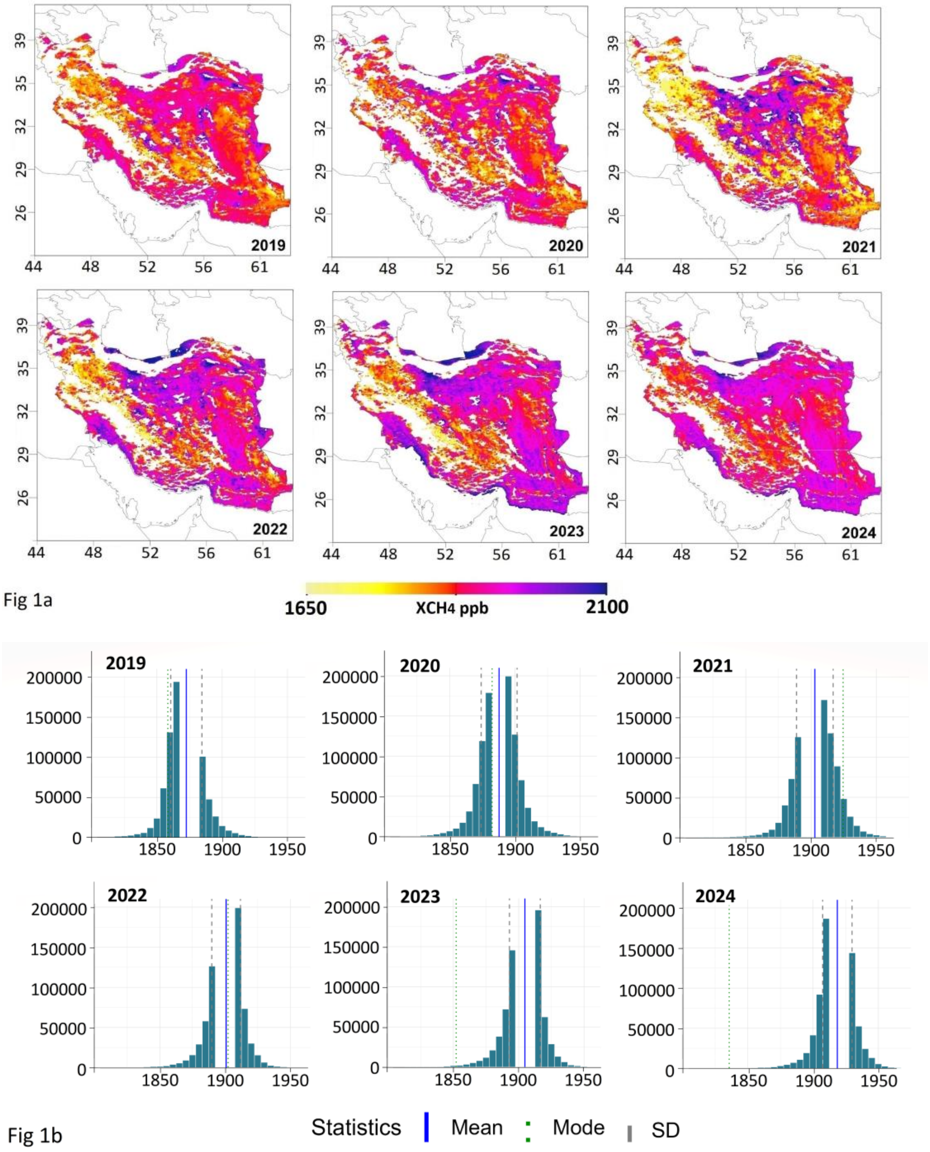

**Figure 1: Annual variations of column-averaged methane over Iran during 2019–2024: (a) Spatial distribution of $XCH_4$ over Iran derived from TROPOMI observations (ppb). (b) Histogram of $XCH_4$ with annual mean and median values.**

205 To investigate the spatial structure of methane concentrations in Iran during 2019–2024, two complementary spatial autocorrelation techniques were employed. The Global Moran's I index was calculated for each year, revealing consistently strong and statistically significant positive spatial autocorrelation across the country (Figure S2). Moran's I values ranged from 0.914 in 2020 to 0.982 in 2024, indicating that areas with high methane concentrations cluster together, while low-concentration areas similarly form cohesive clusters ($p < 0.01$).

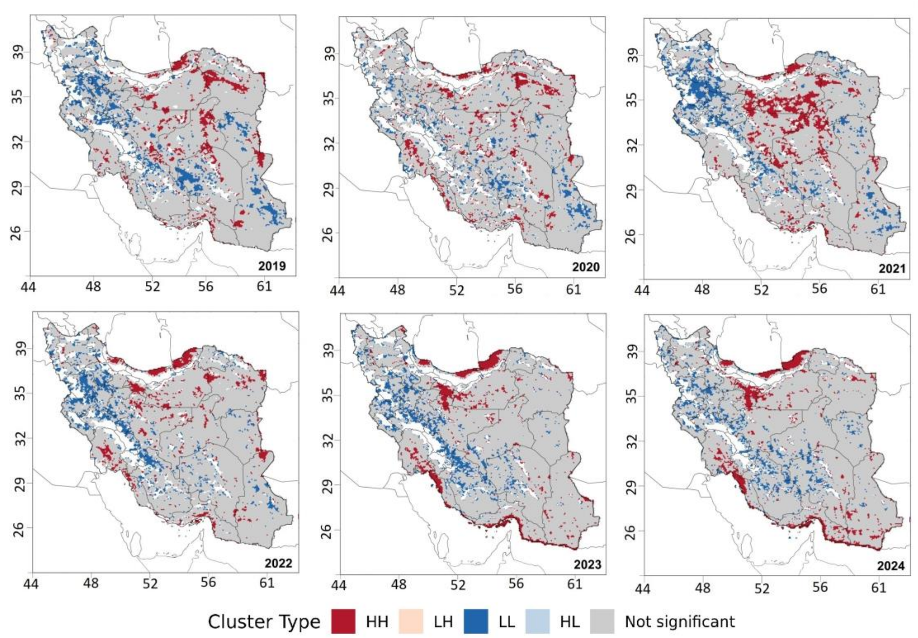

**Figure 2: Local Moran's I cluster map indicating high-high (hotspot) and low-low (cold spot) areas of methane emissions.**

The Local Moran's I, which is a type of LISA, was applied to identify local clusters and spatial outliers at both macro- and micro-levels. Figure 2 shows High-High clusters (red) in regions with intensive industrial, agricultural, or urban activities and Low-Low clusters (blue) in natural or sparsely populated areas. High-Low and Low-High points highlight spatial outliers, reflecting unique environmental conditions or isolated emission events.

To further refine hotspot detection, the Getis-Ord Gi* local spatial autocorrelation index was used. Grid cells with $Z > 1.96$ were identified as statistically significant hotspots, visualized in Figure 3a, while Figure 3b illustrates the actual emission intensity values for these regions. High-emission clusters are concentrated in areas with intensive anthropogenic activities and represent key locations for environmental monitoring and mitigation strategies.

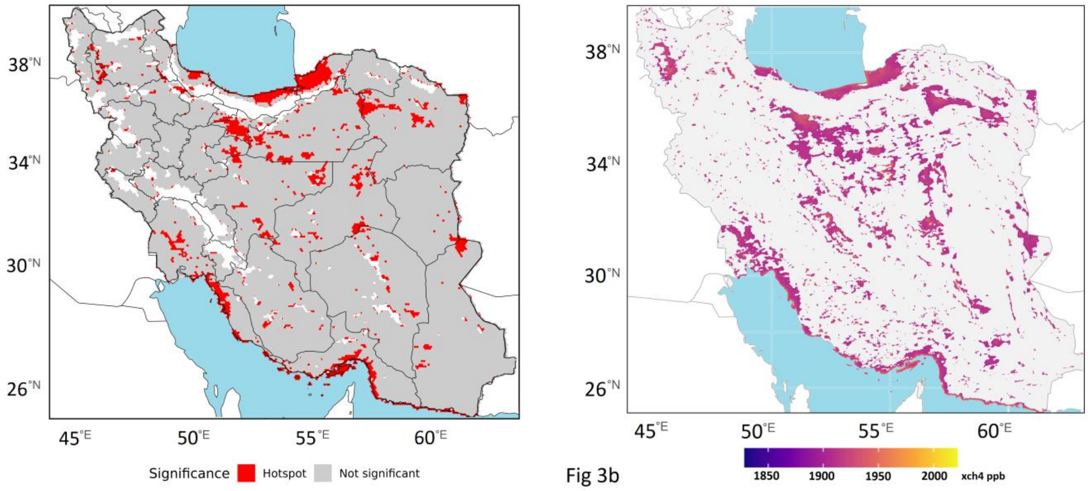

Fig 3b

**Figure 3: Spatial hotspot analysis of methane over Iran during 2019–2024: (a) Hotspot clusters derived from the Getis-Ord Gi* index, where red-toned areas ($Z > 1.96$) represent statistically significant methane hotspots. (b) Actual emission intensity values associated with the identified hotspot regions, based on TROPOMI observations.**

the combined evidence from Moran's I, LISA, and Gi* demonstrates that methane emissions in Iran exhibit a strong and statistically significant spatial clustering pattern rather than random dispersion. Identifiable hotspots and cold spots correspond to human and environmental drivers, including emission sources, urbanization, topography, and meteorological dynamics. Integration of Gi* with Moran's I and LISA provides a robust framework for capturing the spatial dynamics of greenhouse gas emissions at the national scale and supports the design of targeted mitigation strategies, particularly for climate change mitigation and atmospheric pollution control.

### 3.1.2 Provincial Methane Distribution Patterns in Iran

The spatial distribution of methane across Iranian provinces exhibits pronounced heterogeneity, shaped by land use, industrial activity, population density, and climatic conditions. When considering both annual mean $XCH_4$ and hotspot density relative to provincial area, five distinct emission regimes emerge, highlighting the interplay between regional sources and land area The provincial map is shown in Figure S3, and the related statistics are provided in Table S3.

#### 3.1.2.1 Northern Agro-Hotspots

Provinces in northern Iran, namely Golestan, Mazandaran, and Gilan, exhibit elevated methane concentrations driven primarily by wetland rice cultivation and anaerobic decomposition in saturated fields during planting and harvesting seasons (Asadkhani et al., 2025). Annual mean $XCH_4$ ranges from 1880 to 1915 ppb, with a substantial number of emission hotspots concentrated in relatively small areas. Golestan hosts approximately 13,595 hotspots over 20,205 km², Mazandaran 7,044 hotspots across 23,725 km², and Gilan 4,055 hotspots within 14,086 km². The resulting high hotspot density underscores the role of northern flooded rice fields as primary agricultural methane sources, where even modest provincial areas can contribute significantly to national emissions.

https://doi.org/10.5194/egusphere-2025-5852
Preprint. Discussion started: 11 December 2025

#### 3.1.2.2 Central Urban-Dense Hotspots

In the central provinces, including Tehran, Qom, Alborz, Isfahan, and Fars, methane emissions are elevated due to the convergence of urbanization, industrial activity, and intensive agriculture. Tehran-Alborz contains approximately 10,491 hotspots across 24,647 km², Qom 5,250 over 11,514 km², Isfahan 24,920 within 106,754 km², and Fars 12,550 across 122,779 km². The widespread distribution of hotspots coupled with high $XCH_4$ values highlights these provinces as regions where overlapping anthropogenic and agricultural sources amplify methane emissions.

#### 3.1.2.3 Southern Industrial-Fossil Hotspots

Southern and southwestern provinces, such as Khuzestan, Hormozgan, and Bushehr, display pronounced methane enhancements largely associated with oil and gas extraction, petrochemical industries, and fossil fuel transport, further intensified by gas flaring and venting (Chen et al., 2023). With annual mean $XCH_4$ ranging between 1895 and 1920 ppb, Khuzestan hosts 19,434 hotspots across 63,928 km², Hormozgan 18,606 hotspots over 68,809 km², and Bushehr 10,097 hotspots within 22,766 km². Although the area of these provinces is substantial, the absolute number of hotspots creates concentrated industrial emission zones, demonstrating the importance of anthropogenic activity in shaping regional methane patterns.

#### 3.1.2.4 Low-Emission Provinces

Provinces such as Markazi and Lorestan exhibit moderate methane concentrations with relatively low hotspot density. $XCH_4$ values are slightly lower than the central and southern provinces, and the number of hotspots is limited relative to provincial area, reflecting a combination of cooler climate, smaller urban-industrial footprint, and less intensive agriculture. These provinces act as moderate contributors, with emissions distributed sparsely across their territory.

#### 3.1.2.5 Very-Low-Emission Provinces

Finally, western and eastern provinces, including Chaharmahal and Bakhtiari, Ilam, Kurdistan, Ardabil, South Khorasan, and Yazd, show the lowest methane concentrations, with annual mean $XCH_4$ around 1870–1885 ppb. Hotspot counts are minimal: Chaharmahal and Bakhtiari contains only 91 hotspots, Ilam 250, Kurdistan 510, Ardabil 647 and South Khorasan 4,835. Despite the large land area of some eastern provinces, the low density of hotspots and limited anthropogenic or agricultural activity results in minimal methane accumulation, establishing these regions as cold spots within the national landscape.

By organizing provinces according to hotspot density relative to area, a clear pattern emerges. small northern provinces with intensive agriculture and high-density hotspots dominate methane emissions on a per-area basis, followed by central urban-agricultural provinces, southern industrial zones with absolute high emissions, central smaller provinces with low density, and finally western and eastern cold spots. This hierarchical structure emphasizes the need for region-specific mitigation strategies tailored to both emission intensity and spatial distribution of hotspots.

### 3.2 Temporal Variation of CH4 in Iran

Figure 4 illustrates the temporal distribution of methane emissions, highlighting their variability and dispersion across monthly, seasonal, and annual scales. An examination of monthly averages reveals that methane concentrations reach their highest levels during the second half of the year. August (1916 ppb) and September (1912 ppb) exhibit the highest mean values, whereas February (1863 ppb) and March (1861 ppb) record the lowest concentrations. January 2019 shows a mean of 1864 ppb, while December

https://doi.org/10.5194/egusphere-2025-5852
Preprint. Discussion started: 11 December 2025

2024 reaches 1930 ppb, reflecting the upward trend over the six-year period. This disparity reflects the influence of seasonal dynamics on atmospheric methane behavior.

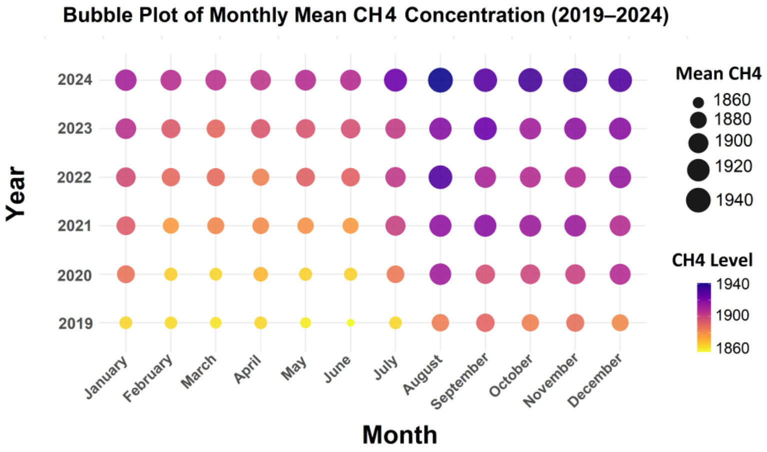

**Figure 4: Monthly and seasonal XCH₄ distribution in Iran (2019–2024)**

In terms of variability, the standard deviation peaks in February 2020 (15.73 ppb) and January 2023 (14.59 ppb), indicating greater instability in the colder months. Nevertheless, the coefficient of variation remains below 1% across all months, ranging from 0.0055 (May 2019) to 0.0084 (March 2020), signifying an overall consistency in the dataset on a broader scale. An analysis of quartiles and the interquartile range (IQR) shows greater dispersion in winter months (e.g., IQR = 20.31 ppb in March 2020), while months like August 2022 (IQR = 13.27 ppb) and October 2023 (IQR = 10.62 ppb) display more uniformity in data distribution (Table S4). A review of extreme values further underscores significant fluctuations in certain months. For instance, December 2023 recorded a minimum of 1645.85 ppb and a maximum of 2141.21 ppb, likely resulting from phenomena such as temperature inversions or localized emissions. In most months, the close proximity of the mean, median, and mode suggests a roughly normal distribution. However, in February, April, and November, discrepancies among these indicators (e.g., February 2024: mean = 1905.91 ppb, median = 1906.66 ppb, Min = 1778.79 ppb, Max = 2120.13 ppb) may point to multimodality or the presence of outliers.

Figure 5 presents the seasonal statistical analysis based on data from the corresponding months of each season over the six-year study period. Winter exhibits the highest interquartile range (IQR = 14.82 ppb) and the widest range of extreme values (Min = 1645.85 ppb, Max = 2141.21 ppb), indicating considerable variability and atmospheric instability during this season. Harsh cold and increased fossil fuel consumption are likely contributing factors. Spring, with an average concentration of 1885.25 ppb and the lowest standard deviation (12.22 ppb), is the most uniform season in terms of data distribution. Enhanced atmospheric ventilation and increased photosynthetic activity during this period may explain the relative reduction in methane levels. Summer shows a mean concentration of 1898.84 ppb, the lowest IQR (12.12 ppb), and standard deviations ranging between 11.09 ppb (June 2024) and 12.53 ppb (August 2020), reflecting relative stability in methane levels. Abundant sunlight and enhanced biological decomposition of organic matter are probable drivers of methane accumulation during this season. Autumn registers the highest seasonal mean at 1909.98 ppb, with standard deviations around 12.77–13.65 ppb, indicating elevated methane concentrations. This may result from leaf fall, reduced photosynthesis, and intensified agricultural activities. A notable gap between the mode and other statistical measures suggests the potential presence of a skewed distribution (Table S5).

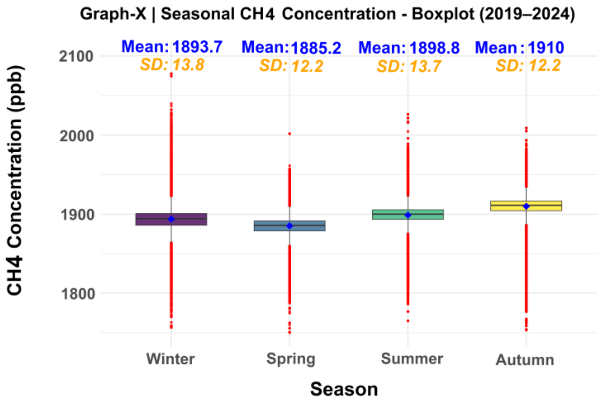

**Figure 5: Seasonal Methane Distribution in Iran (2019–2024)**

Figure 6 illustrates the interannual trend of methane concentrations from 2019 to 2024. The highest recorded concentration (2050.8 ppb) occurred in 2021, likely due to extreme events such as droughts, wildfires, or intensified human activities, while the lowest value (1672.7 ppb) was observed in January 2020. Overall, methane levels in Iran show a pronounced upward trend, with interannual fluctuations reflecting climatic variability and human influences. In 2024, monthly means remained above 1900 ppb, peaking at 1940.95 ppb in August, indicating continued growth (Table S6).

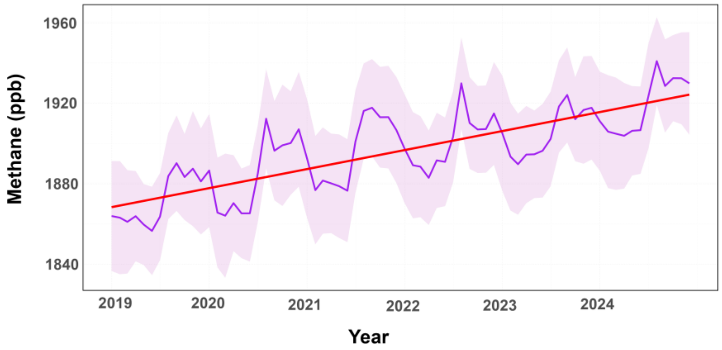

**Figure 6: Interannual variations of $XCH_4$ in Iran (2019–2024)**

## 4 Comparative Analysis of Methane Hotspots in Iran Using TROPOMI Observations and EDGAR v8.1 (2019–2022)

Accurate identification of methane hotspots is critical for targeted mitigation and emission verification. In this study, we compared methane hotspots over Iran using TROPOMI satellite observations and the EDGAR v8 emission inventory for the period 2019–2022, aligning the temporal coverage of both datasets. To facilitate direct spatial comparison, both datasets were resampled onto a common 1 km × 1 km grid. Values from TROPOMI and EDGAR v8 were assigned to the new grid using a nearest-neighbor approach, ensuring that each grid cell accurately reflects the closest original measurement. This high-resolution gridding enables consistent, grid-to-grid spatial analysis and direct comparison of methane concentrations between the two datasets.

https://doi.org/10.5194/egusphere-2025-5852
Preprint. Discussion started: 11 December 2025

Figure 7. Spatial distribution of methane hotspots (high concentrations) and cold spots (low concentrations) across Iran during different months of the year for 2019–2022, based on TROPOMI observations and EDGAR v8.1 monthly sector-specific grid maps. The figure provides a comparative analysis of the two datasets. Seasonal hotspots and cold spots of methane from TROPOMI observations and EDGAR v8.1 inventory are shown for winter (DJF), spring (MAM), summer (JJA), and autumn (SON). TROPOMI consistently identified hotspots in northern provinces (Gilan, Mazandaran, and Golestan), southwestern and southern regions dominated by large-scale oil and gas industrial activities (including extraction wells and refineries), as well as in densely populated central cities of Iran, where human activities contribute to elevated methane emissions. In contrast, EDGAR v8.1 shows hotspots scattered across northern, northwestern, western, and southwestern provinces, and exhibits a relatively stable pattern of cold spots in central and eastern Iran throughout the year.

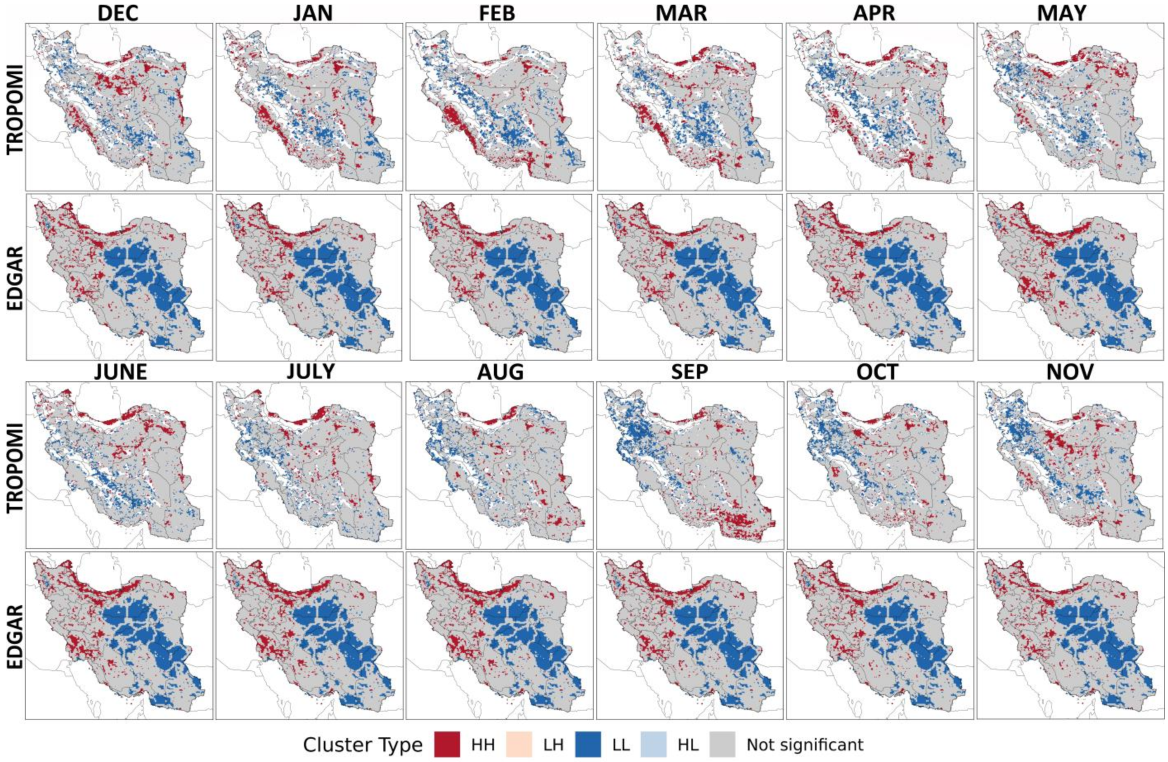

**Figure 7: Seasonal hotspots and cold spots of methane based on TROPOMI satellite observations and EDGAR v8.1 inventory for winter (DJF), spring (MAM), summer (JJA), and autumn (SON) over Iran during 2019–2022.**

To quantify the degree of spatial agreement, the monthly hotspots detected by TROPOMI and EDGAR v8.1 were compared, and the results are presented in Figure 8. For this purpose, grid cells were categorized into four classes: code 1 – significant in both TROPOMI and EDGAR, code 2 – non-significant in both datasets, code 3 – significant only in TROPOMI, and code 4 – significant only in EDGAR (Table S7). On the maps, blue areas indicate hotspots detected only by TROPOMI (Code 3), green areas indicate hotspots detected only by EDGAR (Code 4), red areas represent hotspots detected by both datasets (Code 1), and grey areas denote non-significant grid cells (Code 2). The comparison reveals notable spatial differences between the two datasets. Across all months, the majority of grid cells fell into Code 2 (approximately 68–73% per month), indicating a general lack of agreement in areas with methane emission hotspots. Code 1 cells accounted for only 2.4–3.6% of the grids, reflecting a low level of agreement between the two datasets in identifying hotspots. Most of these agreed-upon hotspots were located in regions with agricultural activity in northern Iran. In contrast, Code 3, representing hotspots detected exclusively by the TROPOMI sensor, comprised about 14–16% of the grid cells, while Code 4, representing hotspots detected exclusively by the EDGAR dataset, accounted for approximately 9–14%.

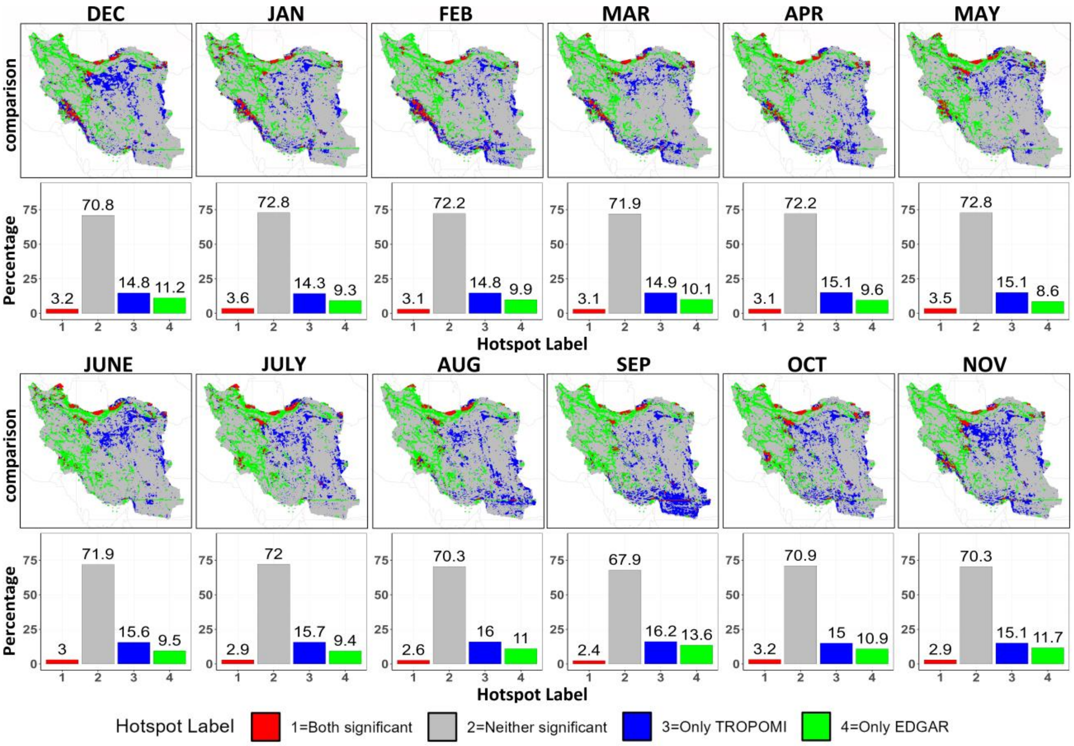

**Figure 8: Seasonal hotspot comparison of TROPOMI satellite observations and EDGAR v8 inventory over Iran (2019–2022)**

Given the pronounced discrepancies between TROPOMI and EDGAR v8.1 in detecting monthly methane emission hotspots in Iran, a comparative analysis reveals three principal divergences: spatial distribution, temporal variability, and emission sources. Spatially, EDGAR v8.1 hotspots are predominantly concentrated in western and northwestern Iran. Despite substantial agricultural activity, including flooded rice cultivation in the three northern provinces, and the presence of major urban centers, such as Tehran and Isfahan, in central Iran, as well as most oil and petrochemical facilities in the south and southwest, The EDGAR v8.1 gridded dataset exhibits limited capability to accurately identify methane hotspots and their spatial distribution.

Temporally, although EDGAR v8.1 partially captures seasonal emissions associated with flooded rice cultivation in northern Iran, it fails to represent the observed temporal variability of methane emissions in this region or across other parts of the country. In contrast, TROPOMI detects substantial methane emissions primarily during summer and autumn, whereas EDGAR v8.1 follows a largely static spatial-temporal pattern.

Regarding emission sources, EDGAR v8.1's monthly sector-specific grid maps categorize methane emissions in Iran into eight sectors, with fuel exploitation accounting for 80.6% of total emissions, agriculture approximately 17%, and the remaining sectors contributing negligibly (Table S2). Conversely, TROPOMI observations indicate that significant methane emissions originate from northern agricultural provinces and densely populated urban areas, including Tehran, suggesting that contributions from agriculture, transport, and building-related waste energy are systematically underestimated in EDGAR v8.1. These findings underscore the necessity for refined sectoral assessments to accurately quantify the relative contributions of different emission sources in Iran.

Several studies have compared satellite-based observational data, which detect atmospheric greenhouse gas concentrations, with inventory datasets such as EDGAR, highlighting discrepancies between reported and observed values. In the context of oil and gas exploitation, livestock production, flooded rice cultivation, and agricultural emissions, analyses have shown that EDGAR tends to underestimate methane emissions when compared with satellite-based or inversion-derived estimates (Maasakkers et al., 2016; Liu et al., 2021; Shen et al., 2023; Waldmann et al., 2025). Focusing on urban and industrial activities, similar comparisons across national and regional levels reveal that EDGAR underrepresents fine-scale variability and hotspot emissions (Plant et al., 2019; de Foy et al., 2023; Tong et al., 2025). Regarding power generation and transport sectors in the Middle East, recent applications of machine learning downscaling also demonstrate that EDGAR may not fully capture emissions (Alcibahy et al., 2025). Collectively, these studies emphasize that while EDGAR provides valuable baseline estimates at global and regional scales, comparisons with high-resolution satellite observations are essential for improving the accuracy of methane emission assessments.

The discrepancies between TROPOMI observations and EDGAR inventories arise from several underlying factors. First, differences in data type and spatial resolution: even after harmonization to a 0.1° × 0.1° grid, EDGAR's modeled emissions may miss fine-scale features. Second, EDGAR has limitations in capturing dispersed or small-scale sources, such as diffuse agricultural emissions or small industrial facilities, because it relies on emission factors (e.g., livestock methane factors, sector-specific coefficients) rather than direct measurements. Third, meteorological influences, including wind speed and direction, atmospheric stability, and vertical mixing, can displace methane plumes and affect satellite detection. Fourth, temporal aggregation effects: TROPOMI captures actual monthly variability, whereas EDGAR relies on annualized emission factors. Finally, minor grid alignment and resampling issues may affect localized hotspot identification.

While EDGAR v8.1 provides consistent, globally scaled emission estimates, TROPOMI captures dynamic spatial variability and additional methane hotspots not represented in the inventory. Combining TROPOMI observations with EDGAR v8.1, along with meteorological variables, land-use information, and supplementary observational constraints, establishes a robust framework for enhancing source attribution, validating emission hotspots, and informing targeted mitigation strategies in Iran. This approach enables the identification of high-confidence hotspots, highlights regions where modeled inventories underperform, and provides a foundation for monitoring temporal and spatial trends in methane emissions, thereby supporting evidence-based, nationally relevant mitigation measures.

## 5 Conclusion

This study demonstrates a significant increase in methane emissions in Iran, highlighting the urgent need for effective mitigation strategies. Spatiotemporal analysis revealed that emissions are not randomly distributed but form statistically significant clusters.

Northern provinces dominated by rice agriculture, central urban-industrial areas, and southern oil–gas regions consistently emerged as major hotspots, whereas western and eastern provinces acted as cold spots. Methane concentrations increased from 1873 ppb in 2019 to 1919 ppb in 2024, with seasonal peaks in late summer and autumn and highest variability during winter months.

Satellite observations from TROPOMI effectively capture actual emissions from all sources, including agricultural and industrial activities, providing high-resolution insights into spatial variability. In contrast, EDGAR v8.1 offers consistent, globally scaled emission estimates but tends to aggregate emissions into broader clusters, potentially underrepresenting dispersed sources, seasonal variations, and fine geographic details. Exclusive reliance on modeled inventories such as EDGAR v8.1 can therefore lead to misidentification or underestimation of critical methane sources, emphasizing the importance of high-resolution observational data for accurate source identification and hotspot verification. For example, EDGAR identifies relatively stable emission centers in the northwest and west, Whereas TROPOMI, in addition to these provinces, also identifies hotspots in central and eastern Iran, so that only Isfahan, Razavi Khorasan, and Semnan have more than 23,000 hotspots each.

Combining TROPOMI observations with EDGAR v8.1, along with meteorological variables, land-use information, and additional observational constraints, provides a robust framework for enhancing source attribution, verifying hotspots, and guiding targeted mitigation strategies in Iran. This approach enables the identification of high-confidence hotspots, highlights regions where modeled inventories underperform, and provides a solid foundation for monitoring temporal and spatial trends in methane emissions, thereby supporting evidence-based, nationally relevant mitigation measures.

Finally, the findings emphasize the value of continuous and precise methane monitoring at regional scales, as emission patterns often transcend national borders. Coordinated data collection and cross-border analysis can enhance the identification of major sources, improve regional and global emission estimates, and inform collaborative mitigation policies. This study narrows the knowledge gap on methane sources and emission patterns in Iran and neighboring countries, providing practical directions for future research, including seasonal predictive modeling, integration of field measurements with satellite retrievals, inverse modeling, and the design of targeted mitigation strategies.

## Data availability

TROPOMI methane data used in this study were obtained via Google Earth Engine. EDGAR 8.1 emission data are publicly available. Any other data supporting the findings of this study are available from the corresponding author upon reasonable request.

## Author contribution

All authors contributed equally to the design of the study, data analysis, and manuscript preparation. CK and MF served as corresponding authors.

## Competing interests

The authors declare that they have no conflict of interest.

## References

Afshoun, H.R., Jabbari, S.M. and Salmani, H.J.: A regional study of the fugitive methane emissions from the gas distribution system in Iran by direct measurement, Journal of Natural Gas Science and Engineering, 105, 104716, doi:10.1016/j.jngse.2022.104716, 2022.

Alcibahy, M., Gafoor, F.A., Mustafa, F., El Fadel, M., Al Hashemi, H., Al Hammadi, A. and Al Shehhi, M.R.: Improved estimation of carbon dioxide and methane using machine learning with satellite observations over the Arabian Peninsula, Scientific Reports, 15(1), 766, doi:10.1038/s41598-024-84593-9, 2025.

Asadkhani, E., Ramroudi, M., Asgharipour, M.R. and Shahhosseini, H.R.: Challenges of sustainability of rice agrosystem: Insights from energy use, ecological footprint, and greenhouse gas emissions (case study: Golestan province, Iran), Agrosystems, Geosciences and Environment, 8(1), e70061, doi:10.1002/agg2.70061, 2025.

Atlantic Council: Climate profile: Iran, [online] Available at: https://www.atlanticcouncil.org/ [Accessed 13 October 2025], 2025.

Chen, Z., Jacob, D.J., Gautam, R., Omara, M., Stavins, R.N., Stowe, R.C., Nesser, H., Sulprizio, M.P., Lorente, A., Varon, D.J. and Lu, X.: Satellite quantification of methane emissions and oil–gas methane intensities from individual countries in the Middle East and North Africa: implications for climate action, Atmospheric Chemistry and Physics, 23(10), 5945–5967, doi:10.5194/acp-23-5945-2023, 2023.

Crippa, M., Guizzardi, D., Pagani, F., Banja, M., Muntean, M., Schaaf, E., Becker, W., Monforti-Ferrario, F., Quadrelli, R., Risquez Martin, A. and Taghavi-Moharamli, P.: GHG emissions of all world countries, Publications Office of the European Union, Luxembourg, 953322, doi:10.2760/173513, 2023.

Darand, M.: Probability changes of observed extreme precipitation events over Iran from 1962 to 2019, Science of The Total Environment, 998, 180298, doi:10.1016/j.scitotenv.2025.180298, 2025.

de Foy, B., Schauer, J.J., Lorente, A. and Borsdorff, T.: Investigating high methane emissions from urban areas detected by TROPOMI and their association with untreated wastewater, Environmental Research Letters, 18(4), 044004, doi:10.1088/1748-9326/acc118, 2023.

Du, M., Kang, X., Liu, Q., Du, H., Zhang, J., Yin, Y. and Cui, Z.: City-level livestock methane emissions in China from 2010 to 2020, Scientific Data, 11(1), 251, doi:10.1038/s41597-024-03072-y, 2024.

ECMWF: Seasonal forecasts, European Centre for Medium-Range Weather Forecasts, [online] Available at: https://www.ecmwf.int/en/forecasts/documentation-and-support/seasonal [Accessed 24 October 2025], n.d.

EDGAR: Emissions Database for Global Atmospheric Research (EDGAR v8.1), Country Profile: Iran, European Commission, Joint Research Centre (JRC), [online] Available at: https://edgar.jrc.ec.europa.eu/country_profile/IRN [Accessed 20 October 2025], 2023.

Ghosh, A. and Manna, S.: Monthly and annual oscillation of methane and ozone in eastern India using Sentinel-5P TROPOMI: Assessment and validation, Environmental Science and Pollution Research, 32(1), 208–225, doi:10.1007/s11356-024-35755-9, 2025.

Gügül, G.N., Yalçın, C. and Özçelik, A.E.: Analysis results of greenhouse gas and meteorology data obtained during pandemic period using developed dynamic monitoring station, In 2023 IEEE East-West Design and Test Symposium (EWDTS), pp. 1–6, IEEE, doi:10.1109/EWDTS59469.2023.10297106, 2023.

Hartmann, D.L., Tank, A.M.K., Rusticucci, M., Alexander, L.V., Brönnimann, S., Charabi, Y.A.R., Dentener, F.J., Dlugokencky, E.J., Easterling, D.R., Kaplan, A. and Soden, B.J.: Observations: atmosphere and surface, In Climate change 2013 the physical science basis: Working group I contribution to the fifth assessment report of the intergovernmental panel on climate change, Cambridge University Press, pp. 159–254, doi:10.1017/CBO9781107415324.008, 2013.

Hernández, O., López, A., Ceron-Cucchi, M.E., AdégbéÏga Alabi, C.D., Loza, C., Juárez Sequeira, A.V., Fissolo, H.M., García, E.M. and Gere, J.I.: Whole Cottonseed as an Effective Strategy to Mitigate Enteric Methane Emissions in Cattle Fed Low-Quality Forages, Animals, 15(6), 819, doi:10.3390/ani15060819, 2025.

Jackson, R.B., Saunois, M., Martinez, A., Canadell, J.G., Yu, X., Li, M., Poulter, B., Raymond, P.A., Regnier, P., Ciais, P. and Davis, S.J.: Human activities now fuel two-thirds of global methane emissions, Environmental Research Letters, 19(10), 101002, doi:10.1088/1748-9326/ad6463, 2024.

Johnson, M.S., Matthews, E., Bastviken, D., Deemer, B., Du, J. and Genovese, V.: Spatiotemporal methane emission from global reservoirs, Journal of Geophysical Research: Biogeosciences, 126(8), e2021JG006305, doi:10.1029/2021JG006305, 2021.

Karimi, N., Sheshangosht, S., Rashtbari, M., Torabi, O., Sarbazvatan, A., Lari, M., Aminzadeh, H., Abolhoseini, S. and Eftekhari, M.: An advanced high resolution land use/land cover dataset for Iran (ILULC-2022) by focusing on agricultural areas based on remote sensing data, Computers and Electronics in Agriculture, 228, 109677, doi:10.1016/j.compag.2024.109677, 2025.

Karoff, C. and Vara-Vela, A.L.: Data driven analysis of atmospheric methane concentrations as function of geographic, land cover type and season, Frontiers in Earth Science, 11, 1119977, doi:10.3389/feart.2023.1119977, 2023.

Kirschke, S., Bousquet, P., Ciais, P., Saunois, M., Canadell, J.G., Dlugokencky, E.J., Bergamaschi, P., Bergmann, D., Blake, D.R., Bruhwiler, L. and Cameron-Smith, P.: Three decades of global methane sources and sinks, Nature Geoscience, 6(10), 813–823, doi:10.1038/ngeo1955, 2013.

Lerner, M.S.: How the USA can feasibly cut methane emissions 30% by 2030: anaerobic digestion of organic waste and various measures in oil and gas production, Biofuels, Bioproducts and Biorefining, 19(2), 267–276, doi:10.1002/bbb.2685, 2025.

Liu, L., Yang, Z.J., Delwiche, K., Long, L.H., Liu, J., Liu, D.F., Wang, C.F., Bodmer, P. and Lorke, A.: Spatial and temporal variability of methane emissions from cascading reservoirs in the Upper Mekong River, Water Research, 186, 116319, doi:10.1016/j.watres.2020.116319, 2020.

Liu, M., Van Der A, R., Van Weele, M., Eskes, H., Lu, X., Veefkind, P., De Laat, J., Kong, H., Wang, J., Sun, J. and Ding, J.: A new divergence method to quantify methane emissions using observations of Sentinel-5P TROPOMI, Geophysical Research Letters, 48(18), e2021GL094151, doi:10.1029/2021GL094151, 2021.

Lorente, A., Borsdorff, T., Butz, A., Hasekamp, O., aan de Brugh, J., Schneider, A., Wu, L., Hase, F., Kivi, R., Wunch, D. and Pollard, D.F.: Methane retrieved from TROPOMI: improvement of the data product and validation of the first 2 years of measurements, Atmospheric Measurement Techniques, 14(1), 665–684, doi:10.5194/amt-14-665-2021, 2021.

Maasakkers, J.D., Jacob, D.J., Sulprizio, M.P., Turner, A.J., Weitz, M., Wirth, T., Hight, C., DeFigueiredo, M., Desai, M., Schmeltz, R. and Hockstad, L.: Gridded national inventory of US methane emissions, Environmental Science and Technology, 50(23), 13123–13133, doi:10.1021/acs.est.6b02878, 2016.

Maazallahi, H., Pourfayaz, F., Irakulis-Loitxate, I. and Avishan, M.: Satellite-based Detection and Quantification of Methane Emissions from Energy and Waste Sectors in Iran (No. EGU25-18300), Copernicus Meetings, doi:10.5194/egusphere-egu25-18300, 2025.

Mahdavian, S.M., Askari, F., Kioumarsi, H., Naseri Harsini, R., Dehghanzadeh, H. and Saboori, B.: Modeling the linkage between climate change, CH4 emissions, and land use with Iran's livestock production: A food security perspective, Natural Resources Forum, 49(3), 2954–2977, doi:10.1111/1477-8947.12532, 2025.

Meyer, A.G., Lindenmaier, R., Heerah, S., Benedict, K.B., Kort, E.A., Peischl, J. and Dubey, M.K.: Using multiscale ethane/methane observations to attribute coal mine vent emissions in the San Juan Basin from 2013 to 2021, Journal of Geophysical Research: Atmospheres, 127(18), e2022JD037092, doi:10.1029/2022JD037092, 2022.

Mousavi, S.M. and Falahatkar, S.: Spatiotemporal distribution patterns of atmospheric methane using GOSAT data in Iran, Environment, Development and Sustainability, 22(5), doi:10.1007/s10668-019-00378-5, 2020.

Najafi, M.S. and Alizadeh, O.: Climate zones in Iran, Meteorological Applications, 30(5), e2147, doi:10.1002/met.2147, 2023.

Nayeb, H., Mirabi, M., Motiee, H., Alighardashi, A. and Khoshgard, A.: A study on estimation of greenhouse gas emissions from industrial wastewater sector in Iran, Journal of Applied Research in Water and Wastewater, 7(1), 64–69, doi:10.22126/arww.2020.4301.1129, 2020.

NOAA: Meteorological versus astronomical seasons, National Centers for Environmental Information, [online] Available at: https://www.ncei.noaa.gov/news/meteorological-versus-astronomical-seasons [Accessed 13 October 2025], n.d.

NOAA: Trends in atmospheric methane (CH4), NOAA Global Monitoring Laboratory, [online] Available at: https://gml.noaa.gov/ccgg/trends_ch4/ [Accessed 13 October 2025], 2025.

Plant, G., Kort, E.A., Floerchinger, C., Gvakharia, A., Vimont, I. and Sweeney, C.: Large fugitive methane emissions from urban centers along the US East Coast, Geophysical Research Letters, 46(14), 8500–8507, doi:10.1029/2019GL082635, 2019.

Prather, M.J., Holmes, C.D. and Hsu, J.: Reactive greenhouse gas scenarios: Systematic exploration of uncertainties and the role of atmospheric chemistry, Geophysical Research Letters, 39(9), doi:10.1029/2012GL051440, 2012.

Qin, X., Tian, H., Canadell, J.G., Shi, Y., Pan, S., Bastos, A., Ciais, P., Crippa, M., Pan, N., Patra, P.K. and Poulter, B.: Greenhouse gas budgets of Central and West Asia (2000–2020): A significant net source to the atmosphere, Global Biogeochemical Cycles, 39(3), e2024GB008370, doi:10.1029/2024GB008370, 2025.

Raziei, T.: Climate of Iran according to Köppen-Geiger, Feddema, and UNEP climate classifications, Theoretical and Applied Climatology, 148, doi:10.1007/s00704-022-03992-y, 2022.

Saunois, M., Stavert, A.R., Poulter, B., Bousquet, P., Canadell, J.G., Jackson, R.B., Raymond, P.A., Dlugokencky, E.J., Houweling, S., Patra, P.K. and Ciais, P.: The global methane budget 2000–2017, Earth System Science Data Discussions, 1–136, doi:10.5194/essd-12-1561-2020, 2019.

Shen, L., Jacob, D.J., Gautam, R., Omara, M., Scarpelli, T.R., Lorente, A., Zavala-Araiza, D., Lu, X., Chen, Z. and Lin, J.: National quantifications of methane emissions from fuel exploitation using high resolution inversions of satellite observations, Nature Communications, 14(1), 4948, doi:10.1038/s41467-023-40671-6, 2023.

South, D.W.: Methane emissions from oil and natural gas operations—30 percent reduction by 2030 possible if domestic and international actions “stay the course”, Climate and Energy, 41(5), 22–27, doi:10.1002/gas.22436, 2024.

Subraveti, S.G. and Anantharaman, R.: Methane enrichment from dilute sources: Performance limits and implications for methane removal and abatement, ChemRxiv, doi:10.26434/chemrxiv-2025-q70cw-v2, 2025.

Talaiekhozani, A. and Nasiri, A.: The modeling of carbon dioxide, methane and non-methane organic gases emission rates in solid waste landfill in city of Jahrom, Iran, SSRN Electronic Journal, doi:10.2139/ssrn.3968310, 2016.

Tong, H., Cheng, T., Li, X., Zhu, H., Ye, X., Fan, D. and Tang, T.: Reduction of methane emissions through improved landfill management, Nature Climate Change, pp. 1–7, doi:10.1038/s41558-025-02391-1, 2025.

Tu, Q., Hase, F., Zhang, Y., Fang, J., Jiang, Y., Li, X., Schneider, M., Yang, Z., Zhang, X. and Li, Z.: Emission characteristics of greenhouse gases and air pollutants in a Qinghai-Tibetan Plateau city using a portable Fourier transform spectrometer and TROPOMI observations, EGUsphere, 1–24, doi:10.5194/egusphere-2025-966, 2025.

United Nations Environment Programme: Global environment outlook: Regional assessment for West Asia, [online] Available at: https://www.unep.org/ [Accessed 13 October 2025], 2022.

Van Geffen, J., Eskes, H., Compernolle, S., Pinardi, G., Verhoelst, T., Lambert, J.C., Sneep, M., Ter Linden, M., Ludewig, A., Boersma, K.F. and Veefkind, J.P.: Sentinel-5P TROPOMI NO2 retrieval: impact of version v2.2 improvements and comparisons with OMI and ground-based data, Atmospheric Measurement Techniques, 15(7), 2037–2060, doi:10.5194/amt-15-2037-2022, 2022.

Waldmann, P., Eckl, M., Knez, L., Gottschaldt, K.D., Fiehn, A., Mallaun, C., Galkowski, M., Kiemle, C., Hutjes, R., Röckmann, T. and Chen, H.: Quantifying agricultural N2O and CH4 emissions in the Netherlands using an airborne eddy covariance system, EGUsphere, 1–38, doi:10.5194/egusphere-2025-3297, 2025.

Xing, Y. and Wang, X.: Impact of agricultural activities on climate change: A review of greenhouse gas emission patterns in field crop systems, Plants, 13(16), 2285, doi:10.3390/plants13162285, 2024.

Zhang, B., Tian, H., Ren, W., Tao, B., Lu, C., Yang, J., Banger, K. and Pan, S.: Methane emissions from global rice fields: Magnitude, spatiotemporal patterns, and environmental controls, Global Biogeochemical Cycles, 30(9), 1246–1263, doi:10.1002/2016GB005381, 2016.

Zhang, J., Han, G., Mao, H., Pei, Z., Ma, X., Jia, W. and Gong, W.: The spatial and temporal distribution patterns of XCH4 in China: New observations from TROPOMI, Atmosphere, 13(2), 177, doi:10.3390/atmos13020177, 2022.